Monthly Notices of the ROYAL ASTRONOMICAL SOCIETY

MNRAS **527,** 2816–2830 (2024) https://doi.org/10.1093/mnras/stad3382
Advance Access publication 2023 November 3

Star formation history of the post-collisional Cartwheel galaxy using *AstroSat*/UVIT FUV images

Y. D. Mayya [1]★ Sudhanshu Barway [2]★ V. M. A. Gómez-González [3] and J. Zaragoza-Cardiel [1,4,5]

[1]*Instituto Nacional de Astrofísica, Óptica y Electrónica, Luis Enrique Erro 1, Tonantzintla, 72840 Puebla, Mexico*
[2]*Indian Institute of Astrophysics (IIA), II Block, Koramangala, Bengaluru 560 034, India*
[3]*Institute for Physics and Astronomy, Universität Potsdam, Karl-Liebknecht-Str 24/25, D-14476 Potsdam, Germany*
[4]*Consejo Nacional de Humanidades, Ciencias y Tecnologías, Av Insurgentes Sur 1582, 03940 Mexico City, Mexico*
[5]*Centro de Estudios de Física del Cosmos de Aragón (CEFCA), Plaza San Juan 1, E-44001 Teruel, Spain*

Accepted 2023 October 27. Received 2023 October 7; in original form 2023 January 12

ABSTRACT

We present the results obtained by analysing the new *AstroSat* Ultra-Violet Imaging Telescope (UVIT) far-ultraviolet (FUV) image of the collisional-ring galaxy Cartwheel. The FUV emission is principally associated with the star-forming outer ring, with no ultraviolet detection from the nucleus and inner ring. A few sources are detected in the region between the inner and the outer rings, all of which lie along the spokes. The FUV fluxes from the detected sources are combined with aperture-matched multiband photometric data from archival images to explore the post-collision star formation history of the Cartwheel. The data were corrected for extinction using A_V derived from the Balmer decrement ratios and commonly used extinction curves. We find that the ring regions contain stellar populations of a wide range of ages, with the bulk of the FUV emission coming from non-ionizing stars, formed over the last 20–150 Myr, that are ∼25 times more massive than the ionizing populations. On the other hand, regions belonging to the spokes have negligible current star formation, with the age of the dominant older population systematically increasing as its distance from the outer ring increases. The presence of populations of a wide range of ages in the ring suggests that the stars formed in the wave in the past were dragged along it to the current position of the ring. We derive an average steady star formation rate, SFR = 5 $M_\odot$ yr^{-1}, over the past 150 Myr, with an increase to ∼18 $M_\odot$ yr^{-1} in the recent 10 Myr.

Key words: galaxies: individual: ESO 350−G040 or Cartwheel – galaxies: star clusters: general.

1 INTRODUCTION

Collisional ring galaxies are a class of star-forming galaxies that form most of their stars currently along a galaxy-sized (several kiloparsecs) ring (Appleton et al. 1996). The Cartwheel galaxy is considered as an archetype for this phenomenon (Marcum, Appleton & Higdon 1992), where the star-forming ring measures 44 kpc in diameter (ring diameter 72 arcsec; distance 125 Mpc using $H_0 = 71$ km s^{-1} Mpc^{-1}; scale: 1 arcsec = 600 pc). Coherent star formation over such a large scale requires a triggering mechanism. It was demonstrated by Lynds & Toomre (1976) that the trigger comes from an outwardly propagating density wave, which is set in when a compact galaxy plunges in to a large gas-rich disc galaxy, almost perpendicular to the disc with the point of impact close to its centre. As the wave moves outward radially, it compresses the gas and triggers star formation along a circular ring, leaving behind an aging stellar population in its wake.

The Cartwheel has been used as a testbed of the predictions of the collisional scenario for the formation of ring galaxies (Appleton et al. 1996). Higdon (1995) found the current star formation, as traced by the Hα emission from H II regions, is exclusively confined to the ring. The ring is found to be expanding, with the expansion velocity measured by Fosbury & Hawarden (1977) using optical long-slit spectroscopy being 90 km s^{-1}. Subsequent H I and Fabry–Pérot observations suggest expansion velocity of ∼54 km s^{-1} (Higdon 1996; Amram et al. 1998). Marcum et al. (1992) found in the Cartwheel a radial colour gradient that systematically reddens interior to the ring as expected from an ageing population in the wake of the wave. Appleton & Marston (1997) established such radial colour gradients in other ring galaxies.

Despite the general success of the expanding ring model for the Cartwheel, there are still issues that need to be addressed. One of them is regarding a conclusive evidence of star formation in the past in the zone interior to the ring. If the ring was expanding at the currently observed expansion velocities, the oldest populations would have at the most an age of 450 Myr. Korchagin, Mayya & Vorobyov (2001) found that the colour gradients reported by Appleton & Marston (1997) are too steep for a population age difference expected between the inner parts and the star-forming ring, and the main cause of the colour gradient is an underlying old population. Mayya et al. (2005) carried out 20-cm Very Large Array (VLA) observations to trace the non-thermal radio continuum (RC) emission from the supernova remnants (SNR) left behind by the ageing populations in the wake of

★ E-mail: dmayya@gmail.com (YDM); sudhanshu.barway@iiap.res.in (SB)

the wave, but the RC emission is fainter than expected if the past star formation rate (SFR) interior to the ring was similar to the presently observed rate of 18 $M_\odot$ yr^{-1} in the ring. In addition, they found the RC emission behind the ring is restricted to narrow radial filaments filling only a small fraction of the azimuthal area. On the other hand, only 10–20 per cent of the RC emission in the ring is thermal, suggesting significant contribution to the RC emission from SNRs. Because of the relatively large beam size (4 arcsec = 2.4 kpc) of the 20-cm VLA observations, it was not able to determine conclusively whether the SNRs are coincident or marginally behind (on the inner part of the ring) the position of the present star formation as traced by Hα.

The high angular resolution (0.2 arcsec = 120 pc) and sensitivity offered by the *Hubble Space Telescope* (*HST*) images offer a direct way to trace the population of clusters left behind by the advancing wave (Struck et al. 1996). The *HST* images show more than a hundred of stellar clusters, a great majority of them confined to the ring. The zone interior to the ring has faint star clusters, mostly coincident with the spokes of the Cartwheel (Hernquist & Weil 1993). The relative faintness of these clusters, and the background offered by the spokes and possibly the pre-collisional disc, has hindered the determination of their ages using optical colours.

Nevertheless, the lack of clear evidence of past star formation in the wake of expanding wave has been a concern to the theories of wave-induced star formation. In order to alleviate this problem, Renaud et al. (2018) carried out a detailed hydrodynamical simulations to explain the observed morphology and star formation in Cartwheel-like galaxies. Using an adaptive mesh refinement code they could reach a cell size as small as 6 pc, thus allowing them to capture the physical processes coupling the galactic-scale dynamics with the star formation activity. They found that the stars formed in the expanding wave are carried by the wave as it ploughs through the disc material. According to this recent model, the ring hosts all the stars that are formed in the expanding wave in the post-collisional disc, and the spokes are the channels through which some of these stars and collected gas rain back into the nucleus. Under this scenario, most of the star formation first occurs in the ring before this activity is transferred to the spokes and then to the nucleus.

The conclusions from Renaud et al. (2018) models are drastically different from that of previous simulations, which predict only recently formed stars in the ring, with successively older generation of stars in successively smaller radii. Tracing the location of stellar populations of up to around a few 100 Myr age can differentiate between these different predictions.

Images at ultraviolet (UV) wavelengths are ideally suited to trace star formation in the recent past without the contaminating effects of light from any pre-collisional old stars. This is because, the early and late B stars, which dominate the integrated light up to around a few hundreds of million years after the death of O stars, are still hot enough to provide far-ultraviolet (FUV) photons. Besides, stars later than B-type have strong Balmer jump and contribute insignificantly at the FUV wavelengths. The *Galaxy Evolution Explorer* (*GALEX*), for the first time, provided far- and near-UV images of the Cartwheel. However, its relatively poor spatial resolution inhibited its use to trace the present and past star-forming locations in the Cartwheel. We have obtained new FUV images, which are described below, with point spread function (PSF) of ∼1.5 arcsec (900 pc), which is the typical angular separation of the star-forming complexes in the Cartwheel. We here combine these new FUV images with archival images in the optical and infrared to study the locations of present and past star formation in the Cartwheel.

Table 1. Log of FUV imaging observations in the Cartwheel.

ID	Date (yyyy-mm-dd)	UT start (hh:mm:ss)	Exp. time (s)
a1	2018-11-11	05:10:51	614
a2	2018-11-11	05:22:14	900
a3	2018-11-11	08:25:44	1211
a4	2018-11-11	10:03:11	1583
a5	2018-11-11	11:40:38	1740
a6	2018-11-11	13:18:04	602
b1	2018-12-15	14:08:53	1287
b2	2018-12-15	15:46:19	1287
b3	2018-12-15	17:23:45	1288
b4	2018-12-15	19:01:12	1285
b5	2018-12-15	20:43:42	1001
b6	2018-12-15	22:28:12	506

In Section 2, we present the observations used in this work and the catalogue of compact FUV sources. The photometric analysis and extinction determination are presented in Section 3. In Section 4, we determine the age and mass of the FUV sources using population synthesis models in different diagrams. We discuss the results in Section 5. A summary and our conclusions are given in Section 6.

2 OBSERVATIONAL DATA AND THEIR ANALYSIS

2.1 New FUV data

In this work, we have used data from Ultra-Violet Imaging Telescope (UVIT) onboard *AstroSat*,[1] which is the first Indian Space Observatory launched by the Indian Space Research Organisation (ISRO). UVIT consists of two identical 38 cm coaligned telescopes, one for the FUV channel from 130 to 180 nm and the other for the near-ultraviolet (NUV) from 200 to 300 nm and visible (VIS) channel from 320 to 550 nm, with a field of view of 28 arcmin at a spatial resolution <1.5 arcsec. The FUV and the NUV detectors are operated in the high gain photon counting mode. In contrast, the VIS detector is operated in the low gain integration mode. The FUV and NUV channels have filters and gratings, whereas the VIS channel has filters. The description of UVIT telescope and calibration details can be found in Kumar et al. (2012) and Tandon et al. (2017, 2020).

The Cartwheel galaxy was observed during two epochs: 2018 November 11 and 2018 December 15 (see Table 1 for details of observations) in FUV data in the *F148W* (CaF2; mean λ1481 Å) filter. The orbit-wise data set was processed using the Level-2 (L2) pipeline that gives data products that are readily usable for science, including intensity and error on intensity maps and effective exposure maps. The L2 processing pipeline has been used for the data reduction, which includes (1) extraction of drift in the pointing of the spacecraft and disturbances in pointing due to internal movements and (2) application of various corrections to measured position in the detector for each photon such as differential pointing with respect to a reference frame for shift and adds operation, systematic effects and artefacts in the optics of the telescopes and detectors, exposure tracking on the sky, alignment of sky products from multi-episode exposures to generate a consolidated set and astrometry (Ghosh et al. 2021, 2022). The pipeline astrometry is sometimes inaccurate, so

[1] https://www.isro.gov.in/AstroSat.html

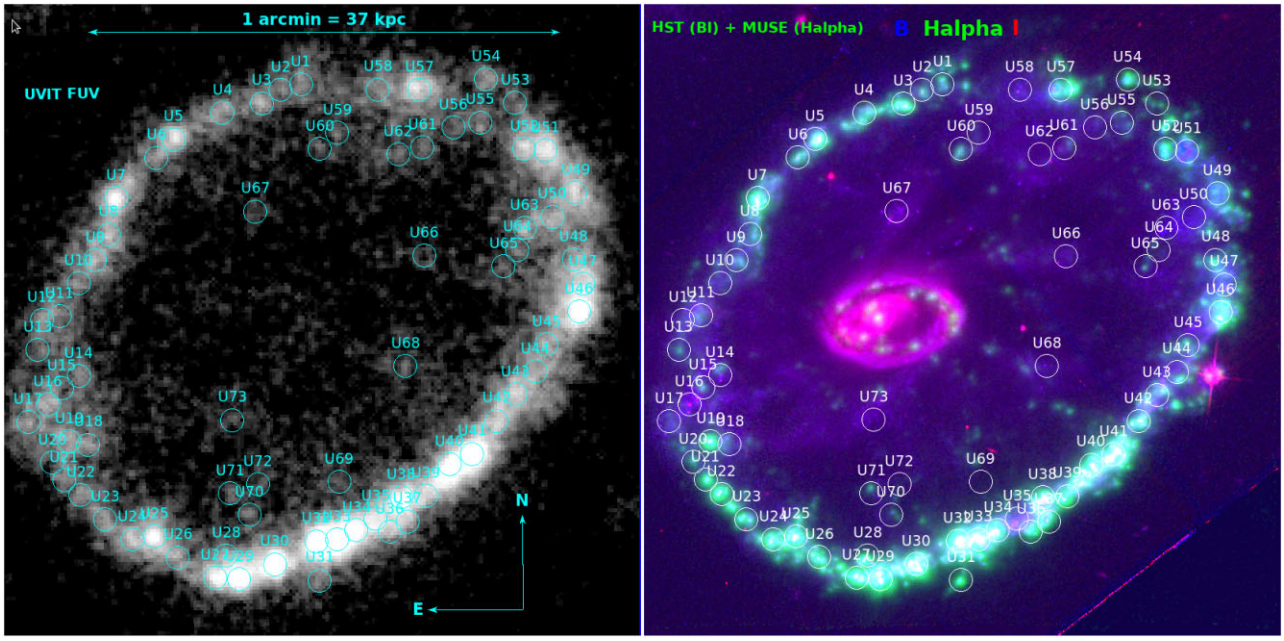

Figure 1. Left: FUV compact sources identified on the UVIT FUV image (cyan circles). Right: RGB colour-composite image formed using *HST*/WFPC2 *F*450*W* (blue), VLT/MUSE Hα (green), and *HST*/WFPC2 *F*814*W* filters. The circles correspond to 1 arcsec radius, which corresponds to 600 pc at the distance of the Cartwheel. Note that all the UV sources lying between the inner and outer rings belong to one of the spokes of the Cartwheel. Scale and orientation are indicated.

we applied our astrometric correction to orbit-wise images using the *GALEX* FUV/NUV tiles. The orbit-wise images are median combined to produce the final deep image shown in the left panel of Fig. 1.

2.2 Compact sources detected on the FUV image

The most easily identifiable characteristic in the UVIT FUV image is the star-forming ring, which is resolved into several individual knots of UV emission. Additionally FUV emission is detected from a few sources along the spokes that connect the outer ring and the nucleus. The nucleus and the inner ring are completely absent in the UV image.

We identified 73 sources on the FUV image, with ∼60 of them belonging to the outer ring or close to it. These sources are identified in Fig. 1 and their equatorial coordinates are given in columns 2 and 3 of Table 2.

2.3 Multiband archival data

We used the available archival data to complement the FUV image from UVIT. These include the Wide Field and Planetary Camera 2 (WFPC2) images in the *F*450*W* and *F*814*W* bands from the *HST* Legacy Archive, Multi-Unit Spectroscopic Explorer (MUSE) spectral cube, and the *K*-band image from the European Southern Observatory (ESO) archive. A summary of the data used in this work is given in Table 3. The tabulated values include the central wavelength and bandwidth, the full width at half-maximum (FWHM) of the PSF, exposure time, the zero-points, and the 3σ limiting magnitudes of each filter. All the magnitudes in this work are presented in the Vega system and accordingly the tabulated zero-points are also in the Vega system. We used the FUV AB zero-point pf 18.08 from Tandon et al. (2020), which was converted to Vega system using the relation $m_{\rm Vega} = m_{\rm AB} - m_{\rm AB}({\rm Vega})$, where $m_{\rm AB}({\rm Vega}) = 2.085$ is the AB magnitude of Vega in the FUV filter, which was taken from Willmer (2018) for the *GALEX* FUV filter.

2.3.1 *Optical continuum and near-infrared images*

The Cartwheel was observed by *HST* in its WFPC2 camera in *F*450*W* and *F*814*W* bands that trace the continuum emission from the stars. These images have a PSF of 0.2 arcsec, which corresponds to 120 pc of physical resolution. The star-forming outer ring is resolved into multiple stellar clusters at this resolution. The zero-points for the *HST* filters were taken from the image headers, which are found to agree within 0.20 mag with the values we obtained from synthetic photometry on the MUSE spectra of bright unsaturated sources common in the *HST* and MUSE field of views. In an earlier work (Barway, Mayya & Robleto-Orús 2020), we have analysed the *K*-band images in the ESO archive to study the morphology of the central bar in the Cartwheel, which are used in this work to carry out photometry on UV-selected regions.

2.3.2 *Hα and Hβ images*

The MUSE data cube was used to generate Hα and Hβ emission line maps. The emission line maps are generated by integrating in filters of 20 Å width around the redshifted wavelengths of Hα and Hβ and subtracting an average of the continuum in windows of 20 Å width. The continuum windows are centred at 37.5 Å on either side of the line, and are free of any emission lines. The archival MUSE data cube is already flux calibrated, and does not require to use zero-points, which is the reason for the blank values in column 7 of Table 3 for the Hα and Hβ filters. The limiting magnitudes are calculated in apertures of 1.5 arcsec radius.

Table 2. Catalogue of compact FUV sources in the Cartwheel[a].

ID	Coordinates (J2000) RA (^{h})	Dec. ($^\circ$)	Photometry m_{FUV} (mag)	em_{FUV} (mag)	M^0_{FUV} (mag)	eM_{FUV} (mag)
1	9.418629	−33.70820	19.897	0.063	−17.109	0.118
2	9.419499	−33.70839	19.959	0.065	−16.776	0.119
3	9.420283	−33.70887	19.612	0.054	−17.372	0.060
4	9.421943	−33.70920	19.599	0.054	−17.525	0.071
5	9.424007	−33.71012	18.855	0.037	−18.149	0.042
6	9.424725	−33.71077	19.640	0.055	−17.337	0.091
7	9.426428	−33.71219	18.557	0.032	−17.819	0.035
8	9.426749	−33.71346	19.175	0.043	−17.594	0.091
9	9.427325	−33.71437	19.311	0.046	−17.305	0.161
10	9.428013	−33.71517	19.885	0.063	−16.731	0.667
11	9.428822	−33.71632	19.840	0.061	−16.776	0.378
12	9.429570	−33.71647	19.746	0.058	−16.870	0.735
13	9.429746	−33.71752	20.291	0.078	−16.325	0.433
14	9.428008	−33.71842	20.033	0.068	−16.583	0.468
15	9.428725	−33.71885	19.894	0.063	−16.722	1.256
16	9.429308	−33.71943	19.369	0.048	−17.248	0.048
17	9.430153	−33.72004	19.674	0.056	−16.942	0.905
18	9.427604	−33.72084	19.742	0.058	−16.984	0.115
19	9.428412	−33.72073	19.383	0.048	−16.826	0.052
20	9.429137	−33.72147	20.064	0.069	−16.588	0.120
21	9.428625	−33.72208	19.933	0.064	−16.435	0.072
22	9.427942	−33.72260	19.808	0.060	−17.062	0.063
23	9.426895	−33.72347	19.653	0.055	−17.053	0.069
24	9.425757	−33.72417	18.924	0.038	−17.556	0.040
25	9.424816	−33.72406	18.427	0.030	−18.083	0.031
26	9.423825	−33.72480	19.465	0.050	−17.500	0.055
27	9.422257	−33.72552	18.373	0.030	−18.081	0.031
28	9.421796	−33.72474	18.830	0.037	−17.459	0.040
29	9.421250	−33.72557	17.851	0.023	−18.623	0.024
30	9.419742	−33.72504	17.870	0.023	−18.669	0.024
31	9.417846	−33.72561	20.197	0.086	−16.419	0.097
32	9.417995	−33.72424	17.432	0.019	−19.224	0.019
33	9.417125	−33.72417	17.338	0.018	−19.149	0.018
34	9.416291	−33.72385	17.846	0.023	−18.712	0.025
35	9.415487	−33.72344	18.282	0.028	−18.334	0.061
36	9.414900	−33.72390	18.781	0.036	−17.906	0.046
37	9.414149	−33.72354	18.802	0.036	−17.714	0.044
38	9.414399	−33.72269	18.126	0.026	−18.320	0.029
39	9.413379	−33.72264	18.603	0.033	−17.899	0.034
40	9.412367	−33.72154	17.819	0.022	−18.469	0.023
41	9.411412	−33.72117	17.597	0.020	−18.886	0.021
42	9.410375	−33.72002	18.834	0.037	−18.154	0.045
43	9.409595	−33.71909	18.795	0.036	−17.821	0.066
44	9.408746	−33.71827	19.177	0.043	−17.439	0.118
45	9.408283	−33.71734	19.247	0.045	−17.369	0.119
46	9.406903	−33.71618	17.955	0.024	−18.782	0.028
47	9.406745	−33.71520	18.392	0.030	−18.224	0.091
48	9.407125	−33.71434	19.120	0.042	−18.420	0.081
49	9.407049	−33.71201	18.784	0.036	−17.832	0.087
50	9.408042	−33.71285	19.242	0.045	−17.374	0.045
51	9.408321	−33.71054	18.477	0.031	−18.139	0.138
52	9.409221	−33.71047	18.804	0.036	−17.941	0.054
53	9.409595	−33.70886	20.150	0.072	−16.466	0.173
54	9.410829	−33.70803	19.848	0.061	−16.431	0.088
55	9.411078	−33.70954	20.110	0.071	−16.506	0.374
56	9.412204	−33.70972	20.511	0.089	−16.105	0.089
57	9.413642	−33.70840	18.802	0.036	−17.846	0.044
58	9.415383	−33.70839	19.732	0.058	−16.884	0.058
59	9.417100	−33.70991	20.929	0.114	−15.688	0.913
60	9.417846	−33.71047	21.219	0.136	−17.043	0.276
61	9.413507	−33.71043	20.864	0.120	−15.752	0.120
62	9.414536	−33.71066	20.827	0.107	−15.789	0.107
63	9.409200	−33.71323	19.560	0.053	−17.056	0.053
64	9.409507	−33.71402	20.362	0.081	−16.254	0.081
65	9.410083	−33.71459	20.865	0.109	−15.751	0.109
66	9.413428	−33.71422	21.761	0.196	−14.855	0.196
67	9.420567	−33.71265	21.625	0.179	−14.991	0.179
68	9.414232	−33.71809	21.140	0.130	−15.476	0.130
69	9.417021	−33.72215	21.156	0.134	−15.460	0.757
70	9.420808	−33.72330	20.880	0.110	−15.736	0.767
71	9.421629	−33.72254	21.372	0.151	−15.244	0.477
72	9.420445	−33.72223	21.321	0.146	−15.295	0.146
73	9.421537	−33.71997	21.446	0.158	−15.170	0.158

Table 2 – *continued*

Note. [a]Vega magnitudes in 1.5 arcsec radius apertures. M^0_{FUV} is the absolute magnitude corrected for extinction using Cardelli, Clayton & Mathis (1989) extinction curve.

Table 3. Description of the multiwavelength data used in this work.

Mission	Filter	λ_c (nm)	$\Delta\lambda$ (nm)	FWHM (arcsec)	T_{exp} (s)	ZP Vega	m_{lim} 3σ
(1)	(2)	(3)	(4)	(5)	(6)	(7)	(8)
AstroSat/UVIT	FUV	148.5	40.2	1.5	13 304	16.00	22.79
HST/WFPC2	*F*450*W*	454.5	78.9	0.20	3200	24.30	24.59
HST/WFPC2	*F*814*W*	793.0	164	0.20	3200	23.65	22.95
VLT/MUSE[a]	Hα	676.4	2	0.60	4030	–	1.4
VLT/MUSE[a]	Hβ	500.8	2	0.60	4030	–	2.5
VLT/ISAAC	*K*	2200	350	0.60	4 × 31	24.19	21.22

Note. [a]The MUSE data cube is used to generate maps in nebular lines Hβ and Hα at their observed wavelengths (λ_c) integrating the line flux in a window of $\Delta\lambda$, and subtracting the average continuum measured at 37.5 Å on either side of the λ_c.The last column for these filters contains 3σ limiting fluxes in units of $\times 10^{-17}$ erg cm^{-2} s^{-1}.

3 PHOTOMETRIC ANALYSIS

3.1 Aperture photometry of compact sources

Though the FUV image provided by the UVIT instrument is the best in spatial resolution at UV wavelengths, it still corresponds to a physical scale of 900 pc given the relatively large distance to the Cartwheel. This scale, nevertheless, is just sufficient to separate the star-forming complexes in the ring of the Cartwheel. We hence chose apertures of 1.5 arcsec radius to carry out photometry in all bands. In order to take into account the vastly different FWHM of the PSFs of the archival images, we resampled all the archival images to the pixel scale of the UVIT image (0.417 arcsec pixel^{-1}) and smoothed them to the resolution of the UVIT image. All the photometry was carried out on these resampled images.

We used the IRAF task PHOT to carry out aperture photometry in concentric circular apertures of radius between 0.5 and 2.5 arcsec in steps of 0.5 arcsec. We used the median value of an annular zone of inner radius and width of 10 and 5 arcsec, respectively, centred on the object as the local background value, and subtracted it from each pixel value, to obtain the magnitude of the source. Note that the chosen annulus is large enough so that the median value is not affected from any contribution from the neighbouring sources in the ring. The instrumental magnitudes are converted to Vega system of magnitudes using the zero-points in column 7 of Table 3. The photometric errors include the photon noise from the source and the background. The magnitude as a function of aperture radius grows

even at the largest aperture of 2.5 arcsec we have used. This is expected for two reasons: (1) the PSF of the smoothed images used for photometry extends beyond the aperture of 2.5 arcsec aperture, and (2) a neighbouring region starts contributing to large apertures due to the crowding of regions. It can be inferred from Fig. 1 that an aperture of 1.5 arcsec radius encloses a complex without getting contribution from neighbouring in almost all cases. We hence chose radius of 1.5 arcsec as the optimum aperture in this study. We found that the colour remains steady as a function of aperture size, in spite of the growth of the magnitude. As we will discuss shortly, the age of the population, which we aim to derive using our data set, is sensitive to colour rather than magnitude and our results are only weakly dependent on the choice of aperture size.

In columns 4–7 of Table 2, we give FUV magnitudes in the Vega system for the identified UV sources. The $m_{\rm FUV}$ is the observed apparent magnitude, whereas the $M^0_{\rm UV}$ is the absolute magnitude corrected for interstellar extinction discussed below. The error on $M_{\rm UV}$ includes error on extinction value at the FUV wavelength and the photometric errors. Table 4 gives the multiband photometric properties of the identified UV sources.

3.2 Determination of A_V

We use the aperture fluxes in continuum-subtracted Hα and Hβ images to calculate the visual extinction using the Balmer decrement method for photoionized nebulae (see Osterbrock & Ferland 2006). We used an intrinsic ratio of $F(\mathrm{H}\alpha)/F(\mathrm{H}\beta) = 2.87$ corresponding to electron temperature and density typical of 10 000 K and 100 cm^{-3}, respectively, for the ionized nebulae. The extinction at the Hβ wavelength is transformed to the visual extinction A_V using the Cardelli et al. (1989) extinction curve. The emission fluxes of Balmer lines, especially the Hβ line, in H II region spectra could be affected by possible Balmer absorption from evolved populations (e.g. González Delgado et al. 2005). Effect of this on the derived A_V is negligible for regions that belong to the outer ring. However, for rest of the regions, especially those having EW(Hβ) < 10 Å, the derived A_V would be overestimated even with this correction. We hence followed the standard procedure (see McCall, Rybski & Shields 1985) of adding 2 Å to the emission EW(Hβ) and recalculated the Hβ flux. The correction for the underlying absorption for the Hα line makes negligible difference to the derived A_V. The errors in fluxes are propagated to obtain errors on A_V.

The resulting distribution of A_V values is shown in Fig. 2. The distribution is asymmetric with a peak and median value of 0.4 mag, and a mean of 0.54 mag. Most of the ring regions have A_V values close to the median value, with the tail that extends up to $A_V = 2.5$ mag corresponding to faint regions in the disc that have EW(Hβ) < 10 Å. Errors on A_V (δA_V) are large for these regions in the tail and hence are not reliable. We hence reset the calculated A_V values with the median value for all regions for which EW(Hβ) < 10 Å. The resulting values of A_V are given in column (14) of Table 4. Column (15) contains the calculated errors.

4 AGE AND MASS OF COMPACT FUV SOURCES

4.1 Evolutionary properties from population synthesis models

In Fig. 3, we show the evolutionary behaviour of FUV luminosity and colours for simple stellar population (SSP) models using the BPASS (version 2.2) code (Eldridge et al. 2017). Standard Kroupa initial mass function (IMF) is used in these models (Kroupa 2001). We show the plots for $Z = 0.004$ metallicity, which corresponds to that of the Cartwheel (Zaragoza-Cardiel et al. 2022). BPASS code calculates all physical quantities not only for single star evolution but also for stellar evolution in binary systems. The left figure illustrates that the UVIT observations are able to detect star-forming complexes as old as ∼200 Myr if they have 10^6 M$_\odot$ of stellar mass. Older clusters need to be more massive to be detected. On the other hand, clusters of even an order of magnitude less mass can be detected if they are younger than ∼10 Myr. All clusters detected in the FUV band can also be detected in the *F*450*W* and *K* bands.

The figure to the right shows the evolution of colours formed from the UVIT and *HST* filters, as well as the equivalent widths (EWs) of Hα and Hβ nebular lines. The latter quantities, referred to as EW(Hα) and EW(Hβ) henceforth, were used from the calculations of nebular line luminosities for the BPASS models by Xiao, Stanway & Eldridge (2018), who carried out the calculations up to an SSP age of 100 Myr. It is worth noting that the evolutionary behaviour of FUV − *F*450*W* colour is almost monotonous over more than 200 Myr of evolution. On the other hand, in any other colour (*F*435*W* − *F*814*W* is shown for illustration), the monotonous reddening with age is interrupted by the red peak at around 10 Myr, which correspond to the appearance of red supergiants (RSGs) in the SSP models. In the SSP models with binary, the red peak is less pronounced. The absence of the RSG-related bump and a higher slope of the FUV − *F*450*W* colour compared to any other colour makes the FUV − *F*450*W* colour an excellent age indicator. EW(Hα) and EW(Hβ) drop abruptly after the first 3 Myr. The expected values are less than 10 Å at 10 Myr for models without binary stars. The presence of binaries extends the duration for which ionizing photons are available which helps to keep the EW(Hα) and EW(Hβ) values marginally above 10 and 3 Å, respectively, even for systems as old as 100 Myr. The figure also illustrates that for a given colour, the age inferred from the binary models is marginally higher than that from single-star models.

4.1.1 Dependence of observed quantities on star formation scenarios

The plotted models in Fig. 3 correspond to the evolution of a single instantaneous burst (IB) of star formation, which is a good approximation for individual star clusters. The aperture diameters used for flux measurement in this study correspond to a physical scale of 1.8 kpc in the Cartwheel. The single-burst scenario is unlikely to be valid over such large scales, especially in a galaxy such as the Cartwheel, which is forming stars for at least the last 80 Myr following the passage of the intruder through the galaxy (Renaud et al. 2018). This interaction is known to have triggered an expanding wave at a velocity of 54 km s^{-1} (Higdon 1996). At this velocity, the chosen aperture is expected to contain stars formed over the last 32 Myr. The spread of ages could be even larger if clusters formed at inner radii were dragged by the wave as it moved outwards (Renaud et al. 2018). Hence, the likely scenario expected in the Cartwheel regions is continuous star formation (CSF; or the presence of star clusters of multiple ages formed over several tens of million years. The observational quantities plotted in Fig. 3 vary over different time-scales, which allows us to determine the ages of the stellar populations in each of the selected regions. For example, the rapid decrease of emission EWs in IB scenario makes diagrams involving EW(Hα) useful for distinguishing between the single burst, multiple bursts, and CSF scenarios. We first make a qualitative comparison of the observed quantities with that expected from different star formation scenarios in colour–magnitude and colour–EW(Hα) diagrams. These diagrams illustrate that a bursty

Table 4. Multiband photometric data of UV sources in the Cartwheel.

ID	B	eB	$U-B$	e$U-B$	$B-I$	eBI	$B-K$	eBK	F(Hα)	SNR		Hα/Hβ	A_V	eA_V	Hα (Å)		Hβ (Å)	
										Hα	Hβ				EW	eEW	EW	eEW
(1)	(2)	(3)	(4)	(5)	(6)	(7)	(8)	(9)	(10)	(11)	(12)	(13)	(14)	(15)	(16)	(17)	(18)	(19)
1	21.12	0.04	−1.22	0.08	0.73	0.10	1.76	0.17	1.028e-15	221	31	3.42	0.54	0.10	83	5	12	1
2	21.06	0.04	−1.10	0.08	0.98	0.08	2.07	0.12	9.998e-16	215	31	3.31	0.44	0.10	75	4	12	1
3	20.43	0.02	−0.82	0.06	0.53	0.06	1.80	0.09	3.764e-15	809	126	3.41	0.54	0.03	255	14	40	2
4	20.94	0.05	−1.34	0.07	0.69	0.10	1.95	0.12	2.083e-15	447	67	3.47	0.59	0.05	199	16	28	2
5	20.01	0.02	−1.16	0.04	0.66	0.04	1.84	0.05	4.836e-15	1040	159	3.42	0.54	0.02	198	6	32	1
6	20.89	0.04	−1.25	0.07	0.83	0.08	2.03	0.09	1.369e-15	295	43	3.41	0.53	0.07	110	7	16	1
7	20.08	0.02	−1.53	0.04	0.54	0.05	1.82	0.05	5.719e-15	1231	206	3.17	0.31	0.02	284	11	46	1
8	20.93	0.05	−1.76	0.06	0.62	0.11	1.98	0.12	1.205e-15	259	39	3.33	0.46	0.08	124	12	16	1
9	20.94	0.05	−1.63	0.07	0.64	0.11	1.47	0.22	7.924e-16	171	20	3.82	0.40	0.16	75	7	8	1
10	21.23	0.06	−1.34	0.09	0.82	0.12	2.36	0.15	3.394e-16	73	4	4.78	0.40	0.75	35	3	2	0
11	20.72	0.04	−0.87	0.07	0.84	0.08	1.40	0.22	5.474e-16	118	8	4.38	0.40	0.40	35	2	2	0
12	20.96	0.05	−1.22	0.08	0.61	0.13	2.01	0.15	3.774e-16	81	4	4.97	0.40	0.85	36	4	1	0
13	21.68	0.11	−1.39	0.13	0.46	0.27	1.59	0.32	3.806e-16	82	7	4.90	0.40	0.46	78	16	6	1
14	21.21	0.05	−1.18	0.09	0.90	0.10	1.89	0.19	2.896e-16	62	6	3.21	0.40	0.40	29	2	3	0
15	20.82	0.04	−0.93	0.07	0.97	0.07	2.02	0.11	4.125e-16	89	2	5.79	0.40	1.70	27	1	1	0
16	20.53	0.03	−1.16	0.06	0.93	0.06	2.08	0.08	1.801e-16	39	3	1.82	0.40	0.00	8	0	1	0
17	20.99	0.05	−1.31	0.08	0.76	0.10	1.62	0.19	2.899e-16	62	3	4.30	0.40	1.08	25	2	1	0
18	20.99	0.05	−1.25	0.08	0.82	0.10	2.12	0.10	9.955e-16	214	31	3.31	0.44	0.10	86	7	13	1
19	20.41	0.03	−1.03	0.06	0.43	0.07	1.53	0.11	4.476e-15	963	166	3.11	0.25	0.02	303	16	55	3
20	21.32	0.06	−1.25	0.09	0.73	0.12	1.82	0.19	9.679e-16	208	31	3.28	0.41	0.10	99	7	16	1
21	20.96	0.03	−1.03	0.07	0.60	0.08	1.51	0.17	2.748e-15	591	99	3.17	0.31	0.03	240	12	44	2
22	20.67	0.01	−0.86	0.06	0.64	0.03	1.44	0.11	4.785e-15	1029	165	3.37	0.49	0.02	364	9	64	1
23	20.81	0.02	−1.15	0.06	0.81	0.03	1.38	0.13	2.222e-15	477	75	3.30	0.43	0.04	162	4	28	1
24	20.11	0.01	−1.18	0.04	0.59	0.03	1.45	0.06	6.887e-15	1477	247	3.21	0.35	0.01	314	7	56	1
25	19.70	0.01	−1.27	0.03	0.46	0.03	1.53	0.04	1.078e-14	2308	386	3.22	0.36	0.01	373	9	63	1
26	20.74	0.03	−1.27	0.06	0.62	0.06	1.84	0.07	4.143e-15	887	139	3.40	0.53	0.02	318	13	51	2
27	19.61	0.01	−1.24	0.03	0.20	0.02	1.46	0.02	1.296e-14	2769	470	3.20	0.34	0.01	571	12	102	2
28	20.69	0.02	−1.86	0.04	0.61	0.05	1.88	0.05	5.150e-15	1104	189	3.14	0.28	0.02	387	15	69	2
29	19.35	0.01	−1.50	0.02	0.36	0.02	1.74	0.02	1.728e-14	3690	621	3.21	0.35	0.01	468	5	83	1
30	19.39	0.01	−1.52	0.02	0.59	0.01	1.90	0.01	1.394e-14	2986	494	3.23	0.37	0.01	327	4	57	1
31	22.84	0.18	−2.65	0.20	1.20	0.28	3.34	0.21	1.797e-15	384	70	3.03	0.17	0.05	614	102	0	9
32	18.44	0.00	−1.01	0.02	0.18	0.01	1.46	0.01	5.141e-14	11 046	1839	3.28	0.41	0.00	761	6	136	1
33	18.86	0.01	−1.52	0.02	0.59	0.01	1.90	0.01	1.921e-14	4129	684	3.21	0.35	0.00	282	2	49	0
34	19.46	0.01	−1.61	0.02	0.62	0.02	1.88	0.02	9.209e-15	1980	322	3.24	0.38	0.01	221	3	38	0
35	19.98	0.01	−1.69	0.03	0.90	0.02	2.11	0.03	2.032e-15	437	57	3.43	0.40	0.06	60	1	8	0
36	20.49	0.02	−1.71	0.04	0.71	0.05	1.81	0.06	3.236e-15	695	108	3.29	0.43	0.03	154	4	25	1
37	20.49	0.03	−1.69	0.04	0.74	0.05	2.01	0.05	3.604e-15	774	125	3.23	0.36	0.03	168	4	30	1
38	19.64	0.01	−1.51	0.03	0.78	0.02	2.23	0.02	6.489e-15	1395	226	3.20	0.34	0.01	165	2	29	0
39	20.04	0.02	−1.44	0.04	0.52	0.04	1.87	0.04	9.121e-15	1961	328	3.22	0.36	0.01	371	8	68	1
40	19.31	0.01	−1.49	0.02	0.54	0.02	1.90	0.02	1.477e-14	3175	543	3.14	0.28	0.01	337	5	60	1
41	19.13	0.01	−1.53	0.02	0.68	0.02	2.07	0.01	1.539e-14	3310	547	3.21	0.35	0.01	248	2	45	0
42	20.10	0.01	−1.27	0.04	0.64	0.03	2.09	0.03	3.721e-15	800	120	3.41	0.54	0.03	149	3	23	0
43	20.10	0.01	−1.31	0.04	0.80	0.03	2.10	0.04	1.972e-15	424	56	3.53	0.40	0.06	72	2	10	0
44	20.40	0.02	−1.23	0.05	0.93	0.03	2.26	0.06	1.193e-15	256	28	3.69	0.40	0.11	38	1	5	0
45	20.54	0.02	−1.29	0.05	0.85	0.04	1.80	0.11	1.134e-15	244	28	3.73	0.40	0.11	50	1	7	0
46	19.50	0.01	−1.55	0.03	0.34	0.02	1.64	0.06	6.298e-15	1352	207	3.31	0.44	0.02	132	2	22	0
47	20.13	0.02	−1.74	0.04	0.47	0.04	1.60	0.12	1.480e-15	318	36	3.67	0.40	0.09	51	1	6	0
48	20.57	0.03	−1.45	0.05	0.41	0.05	1.81	0.14	1.597e-15	343	45	3.65	0.74	0.07	86	3	12	0
49	20.20	0.02	−1.42	0.04	0.31	0.04	1.82	0.08	1.512e-15	325	39	3.60	0.40	0.08	57	1	7	0
50	20.61	0.03	−1.36	0.05	0.56	0.04	2.16	0.08	2.517e-16	54	3	2.73	0.40	0.00	13	1	1	0
51	20.03	0.01	−1.55	0.03	0.14	0.03	1.87	0.05	1.105e-15	237	23	3.68	0.40	0.14	34	1	3	0
52	20.38	0.02	−1.58	0.04	−0.01	0.05	1.74	0.07	2.348e-15	504	76	3.32	0.45	0.04	114	3	18	0
53	21.98	0.03	−1.83	0.08	0.60	0.10	2.21	0.20	5.566e-16	120	19	3.08	0.40	0.16	93	3	18	1
54	21.44	0.02	−1.59	0.06	0.59	0.06	1.69	0.14	1.376e-15	296	49	3.14	0.28	0.06	177	4	32	1
55	21.29	0.03	−1.18	0.08	0.67	0.06	1.67	0.15	3.583e-16	77	8	3.44	0.40	0.39	30	1	4	0
56	21.49	0.06	−0.98	0.11	0.97	0.08	2.07	0.13	1.373e-16	30	3	2.61	0.40	0.00	18	2	2	1
57	20.09	0.02	−1.29	0.04	0.15	0.05	1.87	0.04	3.585e-15	770	121	3.28	0.41	0.03	160	5	26	1
58	20.92	0.04	−1.19	0.07	0.75	0.08	1.85	0.11	1.404e-16	30	3	1.99	0.40	0.00	11	1	1	0
59	21.96	0.09	−1.03	0.15	0.77	0.20	2.96	0.13	1.196e-16	26	3	2.88	0.40	0.46	25	4	3	1
60	22.22	0.13	−1.00	0.19	0.40	0.36	2.52	0.21	4.600e-16	99	13	3.97	1.01	0.25	162	43	20	4
61	21.75	0.07	−0.89	0.14	1.16	0.09	2.43	0.12	1.007e-16	22	3	2.12	0.40	0.00	15	1	2	1
62	21.98	0.08	−1.15	0.13	1.15	0.10	2.39	0.14	7.310e-18	2	3	0.17	0.40	0.00	1	1	3	1

Table 4 – *continued*

ID	B	eB	$U-B$	e$U-B$	$B-I$	eBI	$B-K$	eBK	F(Hα)	SNR		Hα/Hβ	A_V	eA_V	Hα (Å)		Hβ (Å)	
										Hα	Hβ				EW	eEW	EW	eEW
(1)	(2)	(3)	(4)	(5)	(6)	(7)	(8)	(9)	(10)	(11)	(12)	(13)	(14)	(15)	(16)	(17)	(18)	(19)
63	20.64	0.03	−1.08	0.06	0.31	0.05	2.38	0.07	5.414e-17	12	3	0.49	0.40	0.00	2	0	1	0
64	21.98	0.09	−1.62	0.12	0.62	0.16	3.04	0.17	1.343e-16	29	6	1.87	0.40	0.00	23	3	5	1
65	22.18	0.10	−1.32	0.15	0.73	0.16	2.51	0.28	1.545e-16	33	8	1.92	0.40	0.00	44	7	10	2
66	22.32	0.08	−0.56	0.21	1.16	0.13	2.91	0.19	2.428e-17	5	3	0.65	0.40	0.00	7	2	4	1
67	21.50	0.05	−0.13	0.19	1.28	0.07	2.74	0.07	5.675e-18	1	3	0.10	0.40	0.00	1	0	2	1
68	22.12	0.07	−0.98	0.15	0.94	0.14	2.57	0.21	2.240e-17	5	3	0.52	0.40	0.00	5	1	3	1
69	24.59	1.46	−3.43	1.46	1.64	1.69	4.12	1.48	1.030e-16	22	4	3.12	0.40	0.50	165	161	0	41
70	22.95	0.24	−2.06	0.26	1.88	0.28	2.51	0.30	2.036e-16	44	4	5.30	0.40	0.88	168	91	9	3
71	22.44	0.17	−1.07	0.23	0.72	0.36	1.71	0.40	1.871e-16	40	6	2.89	0.40	0.23	70	21	10	3
72	22.71	0.23	−1.38	0.27	0.67	0.48	2.36	0.37	9.067e-17	19	4	2.03	0.40	0.00	37	12	8	3
73	21.69	0.04	−0.25	0.16	1.19	0.08	2.43	0.07	1.377e-17	3	3	0.27	0.40	0.00	2	1	2	1

Note. Columns (2) and (3): *HST F*450*W* (*B*) magnitude and their errors; columns (4)–(9): colours formed from FUV, *F*450*W*, *F*814*W*, and *K* filters followed by their errors; column (10): Hα flux in erg cm^{-2} s^{-1} units; columns (11) and (12): Hα and Hβ signal-to-noise ratio (SNR); column (13): ratio of Hα to Hβ flux; columns (14) and (15): visual extinction in magnitude and error using an equivalent width of 2 Å to correct for the underlying absorption at Hβ (see text for details); columns (16)–(19): Hα and Hβ emission equivalent widths and their errors in Å.

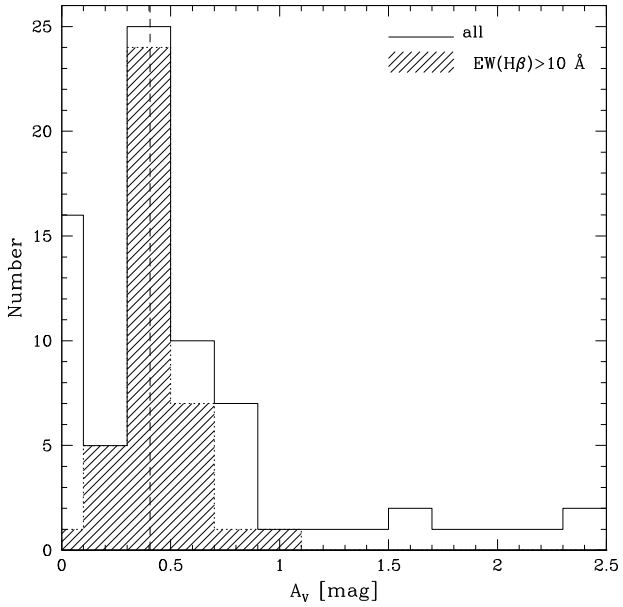

Figure 2. Distribution of A_V (histogram) derived from Balmer decrement of the UV-selected sources. The median value of $A_V = 0.4$ mag is marked by a vertical dashed line. The shaded histogram corresponds to the values for relatively younger regions (EW(Hβ) > 10 Å), where the A_V could be measured using Balmer decrement method, without getting affected by the underlying stellar absorption features.

mode of star formation represents the data better than for a single burst or CSF. We hence adopt a χ^2 fitting to obtain the combination of ages of two representative populations that best reproduce the observed quantities.

4.2 Effect of using different dust extinction and attenuation curves

We used the extinction curve of Cardelli et al. (1989) to obtain A_V values from the Balmer decrement for the regions studies in this work. The Cardelli et al. (1989) extinction curve is known to represent extinction properties from UV to near-infrared along sight lines to different stars in the Milky Way (MW). Gordon et al. (2003) found that the Cardelli et al. (1989) extinction curve is not appropriate in the UV wavelengths ($\lambda < 2000$ Å) along majority of sight lines in the Large and Small Magellanic Clouds (LMC and SMC, respectively). The general tendency is for the UV extinction to be higher than the corresponding value from Cardelli et al. (1989), with the A_{1500}/A_V values reaching values as high as 4.7 for some SMC stars as compared to 2.7 in the MW. Most of the dust causing the extinction to individual stars lies along the line of sight, i.e. in a foreground screen. However, the dust is mixed with the emitting gas in giant star-forming regions, and hence the foreground screen model is a poor approximation when studying extragalactic star-forming regions spread over several hundreds of parsecs. Calzetti, Kinney & Storchi-Bergmann (1994) and Calzetti et al. (2000) characterized the attenuation curves over such large scales and found that the A_{1500}/A_V values are lesser than the corresponding MW values in the nuclei of star-forming galaxies. More significantly, even at the optical wavelengths the extinction suffered by the stellar component was found to be systematically less than that experienced by the nebular gas (see e.g. Calzetti et al. 1994; Mayya & Prabhu 1996). Calzetti et al. (2000) established that typically A_V (cont) $= 0.44A_V$ (gas), where A_V (gas) is the visual extinction derived using Balmer decrement values. This is understood to be due to the destruction of obscuring clouds at the immediate vicinity of the UV and optical continuum-emitting stars by the feedback effects of the massive stars. The nebular flux, on the other hand, originates from larger scales that contain obscuring dust.

The Calzetti et al. (2000) attenuation curve is expected to be appropriate to the UV-emitting sources in the Cartwheel, given that fluxes are measured using aperture diameters of 1.8 kpc. However, given the large variation in the A_{1500}/A_V values in the LMC and SMC and that the Cardelli et al. (1989) extinction curve represents an intermediate value between the SMC and the extragalactic starburst nuclei, we correct the observed values using the Cardelli et al. (1989) extinction curve and show the effects of extinction curves by vectors in all our diagrams, marked by letters SMC, LMC, and C00, which respectively correspond to the average extinction curve from Gordon et al. (2003) for the SMC, 30 Dor star-forming region in the LMC, and the Calzetti et al. (2000) attenuation curve. The plotted vectors show the direction in which the observed points would move if we had used the indicated extinction curve instead of the Cardelli et al. (1989) curve that we have used, with the arrow sizes corresponding

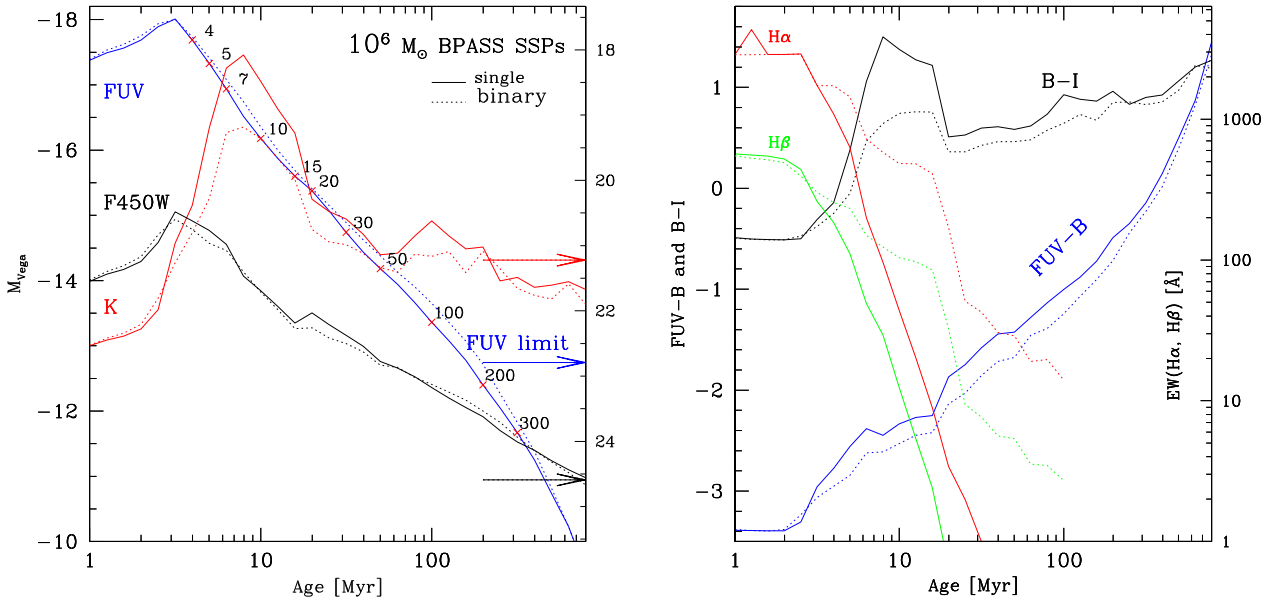

Figure 3. Evolutionary behaviour of quantities used in this work using the BPASS SSP models with (dotted lines) and without (solid lines) binary stars for a metallicity of $Z = 0.004$ and for a stellar mass of 10^6 M$_\odot$. Left panel: absolute magnitudes (left axis scale) in FUV (blue line), optical (*HST F*450*W*; black line), and near-infrared (*K*; red line) filters. Red crosses mark the evolution at selected ages between 4 and 300 Myr. Limiting magnitudes for FUV, *F*450*W*, and *K* magnitudes are also indicated by arrows of colours corresponding to the three filters. Right panel: FUV − *B* and *B* − *I* colours (left axis scale) and Hα and Hβ equivalent widths (right axis scale) are shown by lines of different colours as indicated by the legends. See text for details.

to a nebular extinction of $A_V = 0.4$ mag, which is the average value for our sample.

4.3 Colour–magnitude diagram

In Fig. 4, we plot the photometric properties of the UV-selected regions in a colour–magnitude diagram. Observed values for regions belonging to the star-forming outer ring are shown by empty blue circles, whereas those belonging the spoke and disc regions are shown by solid red circles. These latter points are annotated with their identification numbers to help track their location in different figures. The error bars are plotted for the spoke/disc regions. The sizes of the error bars on the ring regions are typically smaller than the spoke/disc regions, and hence we omit their error bars for the sake of clarity of the figure. BPASS binary evolutionary tracks for SSP populations of 10^7 and 10^6 M$_\odot$ are shown in blue and black lines, with the dashed and solid lines corresponding to the SSPs with and without the binary stars, respectively. The location at specific ages is indicated by a red cross on the 10^7 M$_\odot$ track and is annotated by their ages in million years.

The ring regions are clustered around the track for 10^7 M$_\odot$ between 10 and 50 Myr age. On the other hand, the spoke/disc regions are in general older and less massive. The ring regions are associated with bright ionized nebulae that clearly show signs of the presence of massive hot stars in the form of high-ionization lines such as He II λ4686 (Mayya et al. 2023) and O III λ5007 (Zaragoza-Cardiel et al. 2022). Massive hot stars live for less than ∼5 Myr, and hence it is surprising that none of the ring regions have colours and UV magnitudes corresponding to SSP ages <5 Myr. A different treatment to correct for interstellar dust, and/or the presence of previous generations of stars, is two physical mechanisms that could be the reasons for the observed colours being redder than that expected for an instantaneous burst in its first 5 Myr. We explore these two possibilities below.

The reddening vectors plotted in the figure suggest that the SMC extinction curve would move the points towards ages <5 Myr for majority of the ring regions. On the other hand, the inferred ages would be only marginally younger for the LMC extinction curve, and in fact larger if we had used Calzetti et al. (2000) attenuation curve instead of the Cardelli et al. (1989) extinction curve. Thus, the UV-selected ring regions could be young single-burst populations if the UV extinction curve in the Cartwheel is similar to that for individual stars in the SMC.

Another possibility suggested above is the presence of relatively older generations of stars in the apertures used for measurements. We recall that in the process of obtaining the aperture magnitudes, the contribution from the underlying disc populations has been subtracted out, and hence if an older generation contributes, it should have been formed in the expanding wave. In Fig. 4, we show in dashed green curve the expected locus of a CSF model at a constant rate of 1 M$_\odot$ yr^{-1} for up to 300 Myr. The locus will shift downwards for a lower value of SFR by $\Delta m = 2.5 \log(\mathrm{SFR})$. The observed colours of ring regions correspond to ongoing star formation for 30–300 Myr at rates of 0.025–0.04 M$_\odot$ yr^{-1}.

The colour–magnitude diagram alone cannot distinguish between effect of reddening and the presence of older populations. On the other hand, as we discuss below, plots involving EW(Hα) help to break this degeneracy.

4.4 EW(Hα) versus colour diagram

In order to understand the reasons for the observed FUV − *F*450*W* colours of ring regions being redder than that expected for populations producing copious amount of ionization, we plot in Fig. 5, EW(Hα) against the FUV − *F*450*W* colour. The observed points and the reddening vectors follow the same convention as in Fig. 4. The locus of an IB binary model from BPASS (Eldridge et al. 2017) is shown in solid black line. It may be noted that the EW being the ratio

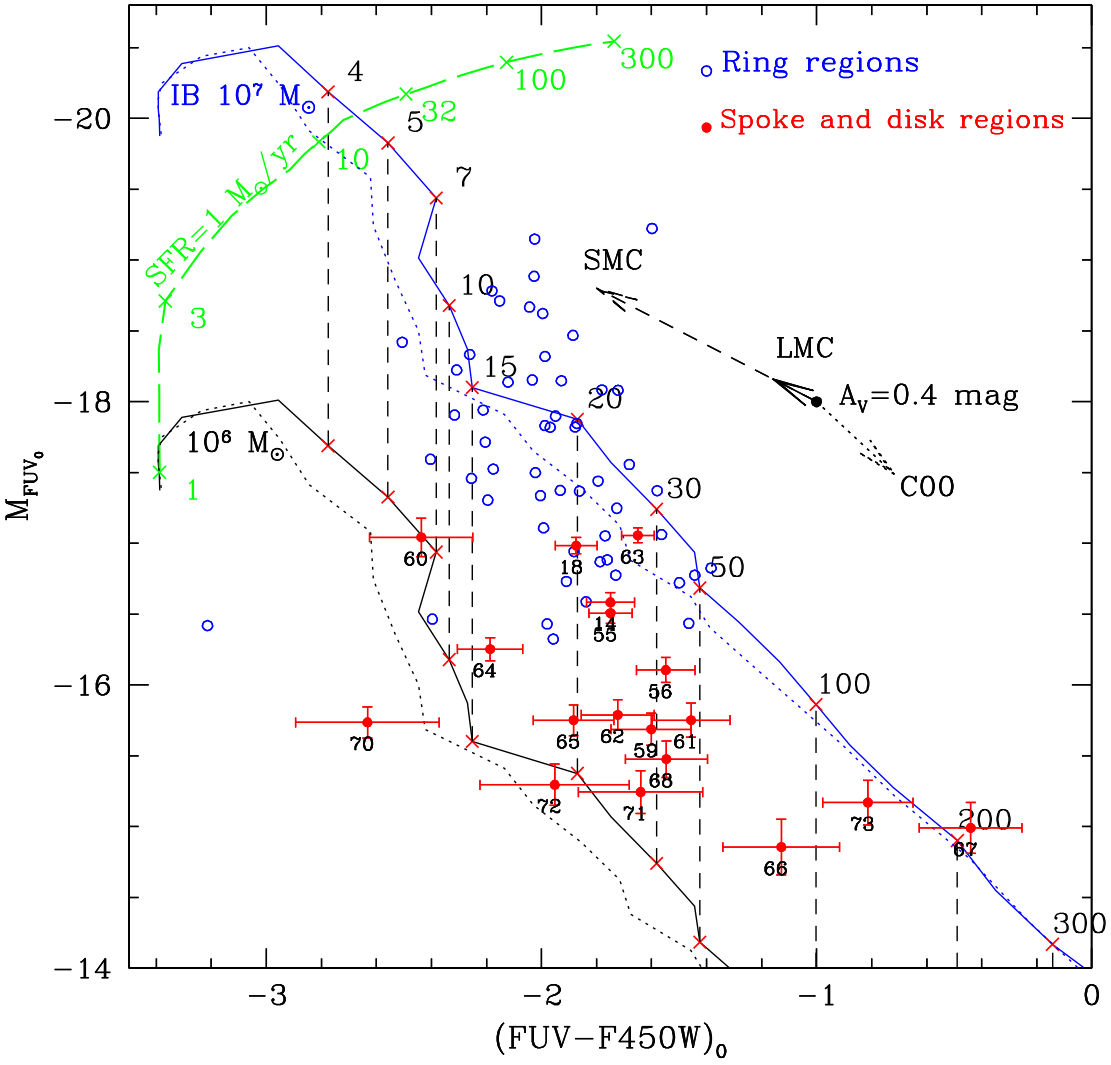

Figure 4. Absolute magnitude ($M_{\rm FUV}$) of the FUV sources located in the ring (blue circles) and the spokes or the inner disc (numbered red dots) plotted against their FUV − *F*450*W* colours. Evolutionary track for clusters of masses 10^7 $M_\odot$ (blue lines) and 10^6 $M_\odot$ (black lines) for single and binary (dotted) SSP models are shown, with the numbers above the cross marks denoting the age in million years. The dashed vertical lines connect the equal-age models for the two plotted cluster masses. The observed magnitudes and colours have been corrected for extinction using A_V and Cardelli et al. (1989) extinction curve. Use of the SMC and LMC extinction curves or the Calzetti et al. (2000) attenuation curve would move the observed points by the amount shown by the arrows marked by letters SMC, LMC, and C00, respectively, for the mean $A_V = 0.4$ mag. The green line shows the effect of star formation proceeding continuously for 300 Myr at a constant rate of 1 $M_\odot$ yr^{-1}, with the tick marks and the associated numbers showing the age in million years. See text for details.

of emission line to continuous fluxes is independent of the cluster mass. It is also independent of extinction if the obscuring dust is in the foreground such as the case for the LMC, SMC, and MW extinction curves. It may have a small dependence on extinction if the absorbing dust is mixed with the gas, and the stars and gas have different spatial extent, as is normally the case in complex star-forming regions (Calzetti et al. 2000). The plot also contains the locus for CSF (green line) and for a model that contains two populations of distinct ages, with the older one contributing negligibly to the ionization (red line). The plotted model corresponds to a 100 Myr old population that is 10 times more massive than the young population of the annotated age. The CSF is carried out for a constant SFR = 1 $M_\odot$ yr^{-1}. However, the observed locus is independent of the SFR as long as it is constant over the plotted duration of 100 Myr.

As illustrated in Fig. 3 (right), the EW(Hα) for the IB model falls rapidly for ages greater than ∼3 Myr, with its value being <10 Å, for ages >100 Myr. The observed EW(Hα) for the ring regions is systematically lower than that expected for populations younger than 16 Myr, with both the observed FUV − *F*450*W* colour and EW suggesting burst ages between 16 and 64 Myr. As noted while discussing the colour–magnitude diagram in the previous section, these ages are too large to explain the high-ionization state of the ring regions. The CSF model provides the required ionization. However, the EW(Hα) for the CSF model lies above 600 Å, the highest value observed for our sample, even after star formation proceeding for 100 Myr. Thus the CSF scenario can be clearly ruled out in all observed regions. On the other hand, existence of an old massive non-ionizing population, such as illustrated by the model represented by the red line, is able to reproduce the observed values of EW(Hα) for the young population ages of 4–10 Myr. The mean of the observed colours of the ring regions is also consistent with the colour of the combined populations. However, there is a spread of 0.5 mag in colour around the mean value. Variation in extinction properties from region to region could be the reason for this dispersion.

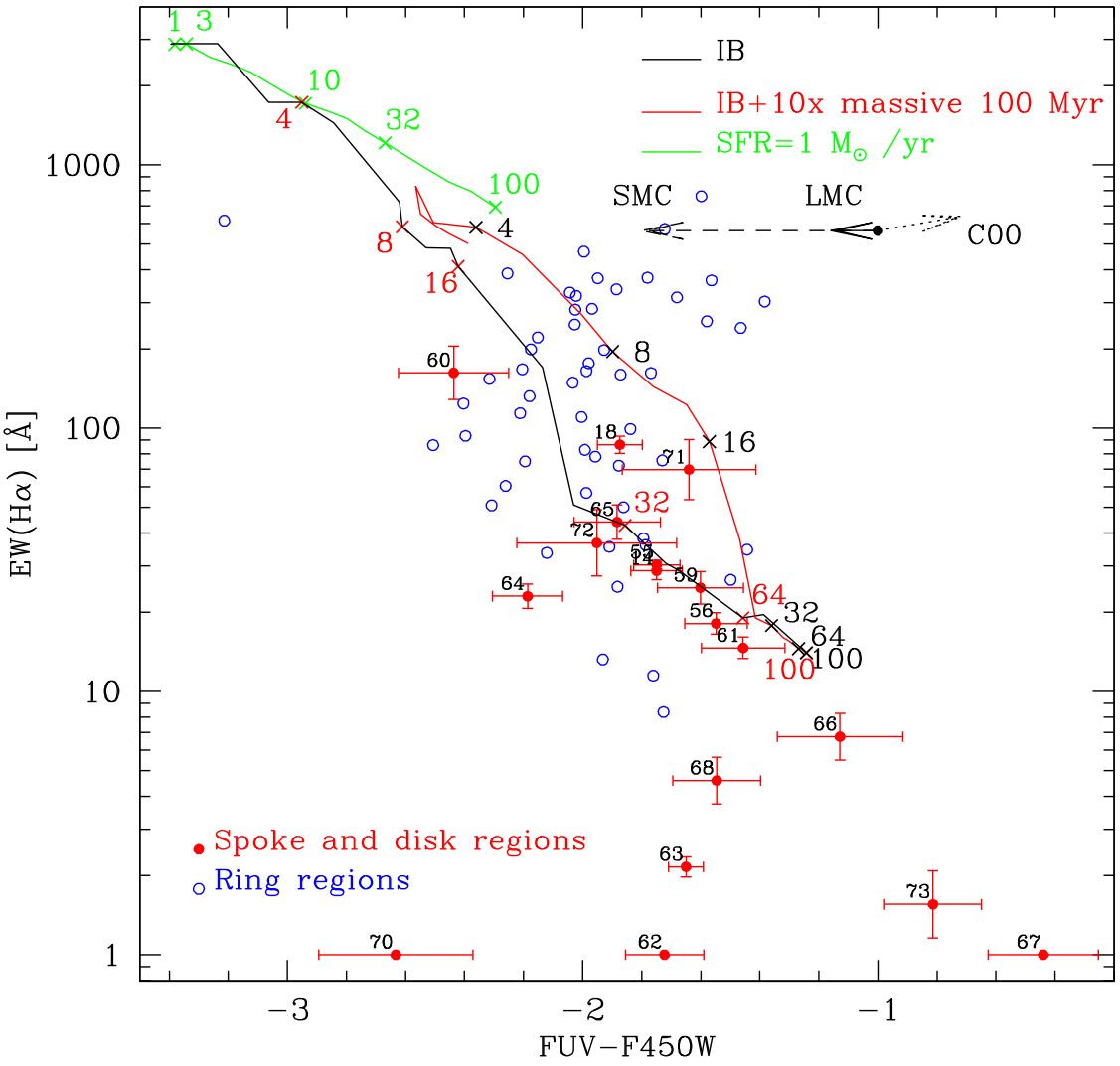

Figure 5. EW(Hα) of the FUV sources located in the ring (blue circles) and the spokes or the inner disc (numbered red dots) plotted against their FUV − *F*450*W* colours. The black and green lines show the trajectory for IB and continuous star formation (CSF) models, respectively, for the BPASS binary tracks. The observed quantities have been corrected for extinction using A_V and Cardelli et al. (1989) extinction curve. Use of the SMC and LMC extinction curves or the Calzetti et al. (2000) attenuation curve would move the observed points by the amount shown by the arrows marked by letters SMC, LMC, and C00, respectively, for the mean $A_V = 0.4$ mag. Effect of a massive (×10) old burst (100 Myr) superposed on bursts of age between 1 and 100 Myr is shown by the red line. Numbers accompanying the tick marks on the model curves indicate the ages in million years.

The EWs and FUV − *F*450*W* colours of the disc and spoke regions (red points) follow the IB evolutionary trajectory until the last available SSP age of 100 Myr, with the majority of points in agreement with the IB scenario between ages of 32 and 64 Myr. Seven regions (ID numbers 62, 63, 66, 67, 68, 70, and 73) that have the lowest observed EWs seem to lie around the trajectory that is obtained by extrapolation of the age <100 Myr track, suggesting ages larger than 100 Myr.

4.5 Best-fitting SSP models

We used a χ^2 minimization procedure to obtain the ages and relative masses of two SSPs whose combined contributions best fit the observed FUV − *F*450*W* colours and EWs. The χ^2 is defined as

$$\chi^2 = \left(\frac{C_{\rm obs} - C_{\rm mod}}{\sigma_{\rm c}}\right)^2 + \left(\frac{\lg {\rm EW}_{\rm obs} - \lg {\rm EW}_{\rm mod}}{\sigma_{\rm ew}}\right)^2, \quad (1)$$

where $C_{\rm obs}$ and $C_{\rm mod}$ are the observed and model FUV − *F*450*W* colours, respectively. Similarly $\lg {\rm EW}_{\rm obs}$ and $\lg {\rm EW}_{\rm mod}$ are the observed and model Hα EWs in logarithmic units, respectively. The error terms $\sigma_{\rm c}$ and $\sigma_{\rm ew} = \log(1 + {\rm err}_{\rm ew}/{\rm EW})$ are the errors in the observed FUV − *F*450*W* colours and EWs, respectively. The model colour and EW are defined as the combined values for the two populations, which depend on the mass and age of the two populations. The observed Hα luminosity and FUV magnitudes, after extinction corrections, are used to constrain the masses of the two populations.

As a first step, we determine the mass of the young population using the observed Hα luminosity and assuming that the entire observed ionizing flux comes from this young population. With this assumption, the error in the determined mass would be less than 10 per cent if the second population is older than ∼10 Myr:

$$\mathcal{M}_{\rm young} = \frac{L({\rm H}\alpha)_{\rm obs}}{L({\rm H}\alpha)_{\rm young}}, \quad (2)$$

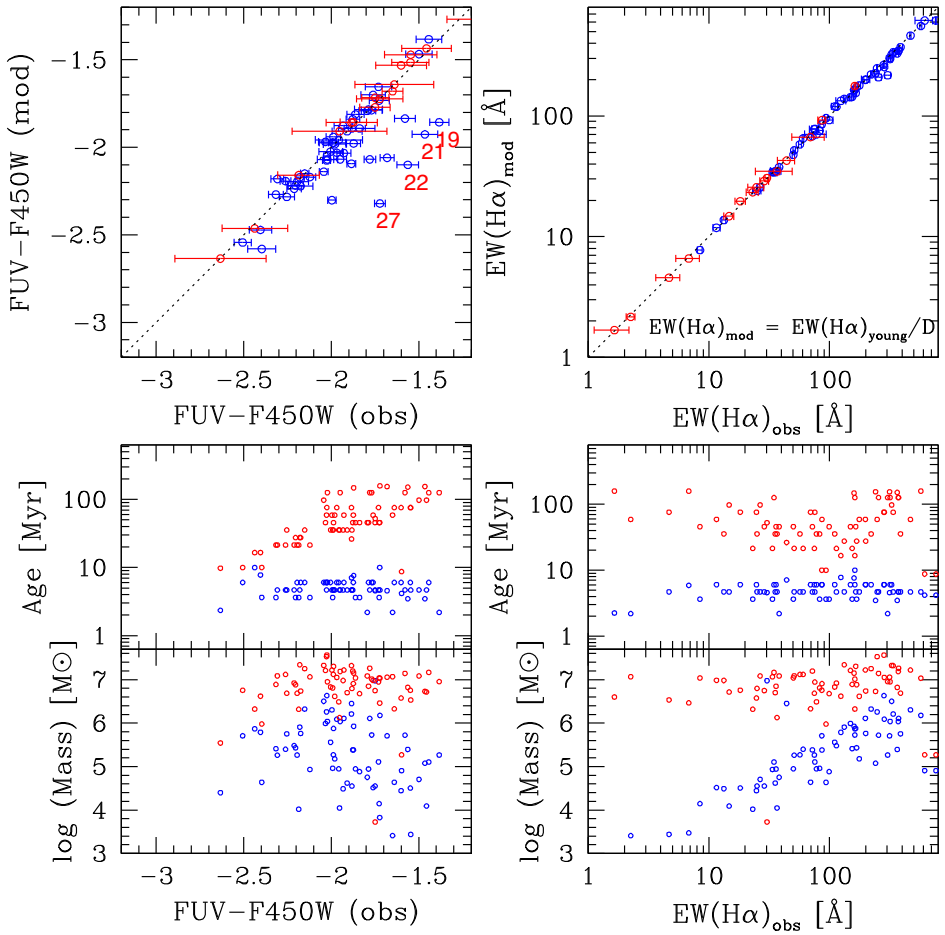

Figure 6. Results of the χ^2-fitting procedure. Top panels: model and observed colours FUV − *F*450*W* (left) and EW(Hα) (right) are compared with that of the two-population models. Bottom panels: individual ages and mass of FUV sources in the ring and spokes of the Cartwheel as a function of observed colour FUV − *F*450*W* (left) and EW(Hα) (right). See Section 4.6 for details.

where $L(\mathrm{H}\alpha)_{\mathrm{young}}$ is the Hα luminosity per unit cluster mass for the binary models of BPASS following the nebular line luminosity calculations of Xiao et al. (2018). We then calculated the FUV luminosity produced by this population and subtracted this from the observed FUV luminosity to estimate the residual FUV luminosity. We obtained the mass of a second older population that correspond to the residual FUV luminosity, as given by the following equation:

$$\mathcal{M}_{\mathrm{old}} = \frac{10^{-0.4M^{0}_{\mathrm{FUV}}(\mathrm{obs})} - 10^{-0.4M_{\mathrm{FUV}}(\mathrm{young})} \times \mathcal{M}_{\mathrm{young}}}{10^{-0.4M_{\mathrm{FUV}}(\mathrm{old})}}. \quad (3)$$

The C_{mod} and $\mathrm{EW}_{\mathrm{mod}}$ in equation (1) are calculated for the combined population using the following equations:

$$C_{\mathrm{mod}} = -2.5\log(L_{\mathrm{FUV}}(2\mathrm{pop})) + 2.5\log(L_{\mathrm{F450}}(2\mathrm{pop})), \quad (4)$$

$$\mathrm{EW}_{\mathrm{mod}} = \frac{\mathrm{EW}(\mathrm{H}\alpha)(\mathrm{young})}{D}, \quad (5)$$

where $L_{\mathrm{FUV}}(2\mathrm{pop})$ and $L_{\mathrm{F450}}(2\mathrm{pop})$ are the sum of the model luminosities in the FUV and *F*450*W* filters from the young and old populations, and $D = L_{\mathrm{H}\alpha\mathrm{c}}(2\mathrm{pop})/L_{\mathrm{H}\alpha\mathrm{c}}(\mathrm{young})$ is the dilution factor of EW(Hα) due to the continuum at the Hα wavelength from the non-ionizing older population.

The age of the second population is constrained to be older than that of the young population. We calculated χ^2 by varying the age of the younger population between 1 and 15 Myr and that of the older population between that of the young population and up to 200 Myr in logarithmic steps of 0.1 dex. The age that gives the minimum χ^2 is stored as the course value of age, t_{course}. In a second iteration the C_{mod} and $\mathrm{EW}_{\mathrm{mod}}$ are interpolated to get their values at logarithmic age steps of 0.01 dex between $\log t_{\mathrm{course}} - 0.1$ and $\log t_{\mathrm{course}} + 0.1$. The χ^2 minimization procedure is repeated to obtain the new age with this fine interval. The masses of the young and old populations corresponding to the best-fitting age are stored.

4.6 Age and mass of FUV sources in the ring and spokes

The results of the χ^2 fits are summarized in Fig. 6. In the top two panels the observed colours and EWs are compared with that of the two-population models. Our χ^2-fitting procedure is able to simultaneously reproduce the observed colours and EWs over the entire range of observed values except for a group of ∼10 regions with FUV − *F*450*W* > −2.0. Five of these having extreme differences are labelled with their identification numbers. These are the same regions that lie to the right of the red line in Fig. 5 (EW(Hα) ∼ 400 Å and FUV − *F*450*W* ∼ −1.5). Differential reddening between stars and gas following Calzetti et al. (2000) is the most likely reason why our χ^2 fitting using Cardelli et al. (1989) was not able to reproduce these values.

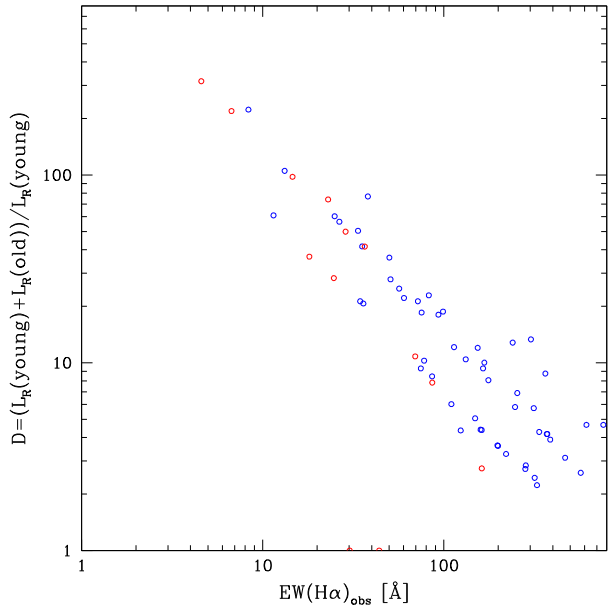

Figure 7. Results of the χ^2-fitting procedure. Dilution factor D (see equation 5) versus the observed EW(Hα) of the UV sources in Cartwheel.

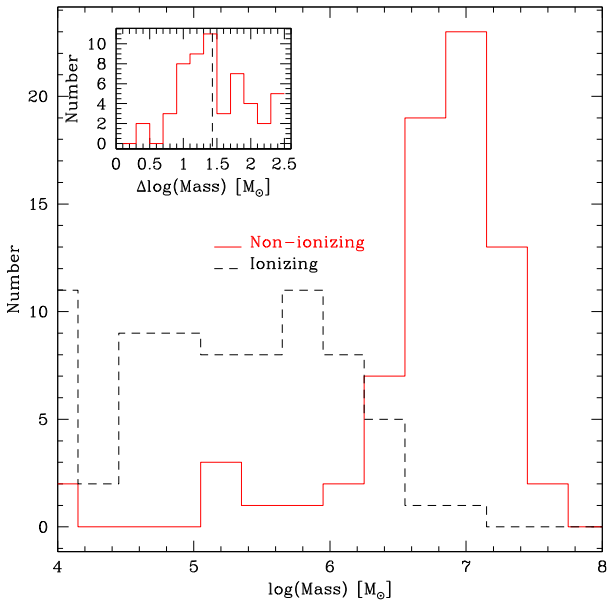

Figure 8. Distribution of masses (histogram) of the non-ionizing (red line) and ionizing (dashed black line) populations in the ring regions of Cartwheel. The non-ionizing population traces relatively older population that has a mean mass of 10^7 $M_\odot$, which is ∼25 times larger than the mean mass of the younger population.

In the bottom panels of Fig. 6, we show the individual ages and masses of the two populations as a function of observed colours and EWs. The age of the older population is proportional to the observed colour, indicating that the FUV − $F450W$ colour has very little contribution from the population that is contributing ionizing photons. This is due to an order of magnitude higher mass of the older population as compared to that of the younger population. The relatively large mass of the non-ionizing population makes the observed EW(Hα) insensitive to the age of the younger population. Instead, the EW is dictated by the mass, or equivalently the Hα luminosity of the younger population, i.e. regions luminous in Hα have systematically higher EW and vice versa. The presence of a dominant older population makes the observed EW(Hα) dependent strongly on the dilution factor D (see equation 5), as is illustrated in Fig. 7.

In Fig. 8, we compare the distribution of masses of the young and old populations. The mean mass of older non-ionizing population is 10^7 $M_\odot$, which is ∼25 times larger than the mean mass of the younger ionizing population (see the inset).

5 DISCUSSION

Having obtained the ages and masses of stellar populations in the outer ring and the disc, including some regions belonging to the spokes, we now analyse the star formation history of the Cartwheel in the context of the collisional model of the formation of the star-forming ring.

5.1 Radial colour gradient

Marcum et al. (1992) found a strong radial colour gradient in Cartwheel that they found to be consistent with a sequential aging of star formation following the ring-making collision. Korchagin et al. (2001) found a non-negligible contribution from the stars belonging to the pre-collisional disc to the observed colour. The radial colour gradient was inferred by Marston & Appleton (1995) using azimuthally averaged colours. The region between the outer and inner rings of the Cartwheel has considerable structures, including the presence of spokes, which makes the azimuthal averaged colours a poor representation of the real variations. We here use our UV-selected sources, without azimuthal averaging, to study the radial gradients in age.

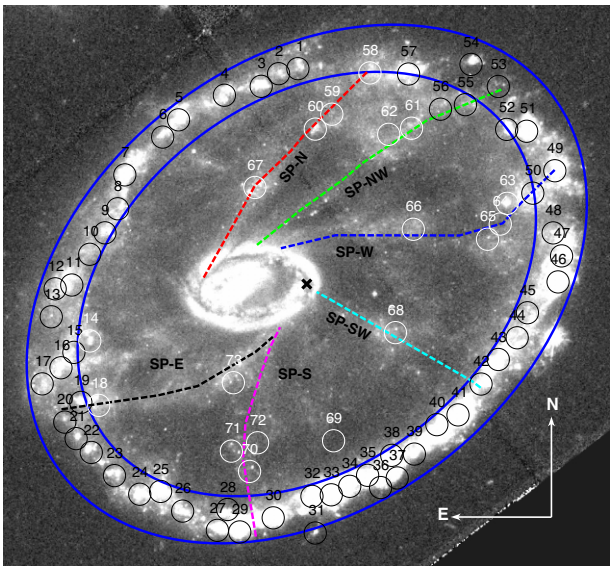

Figure 9. Identification of prominent spokes on the $F435W$ image of the Cartwheel. Dashed lines of different colours are drawn to identify each spoke, which are labelled by letters SP-N, SP-NW, SN-W, SP-SW, SP-S, and SP-E. Two concentric ellipses delimit the UV sources belonging to the star-forming ring (black circles). The back cross shows the ellipse centre. The majority of the UV-selected sources between the inner and outer rings (white circles) belong to one of the six spokes.

In Fig. 9, we illustrate that the majority of the UV-selected sources between the inner and outer rings belong to one of the six spokes

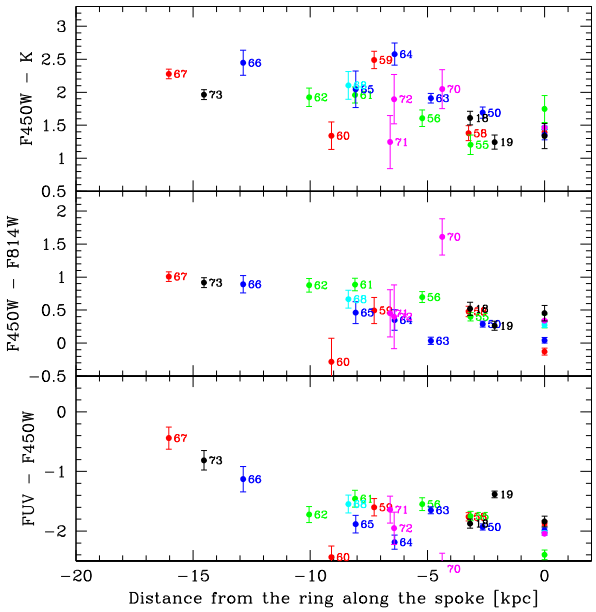

Figure 10. Radial variation of the measured quantities, where the distance is measured along the spoke where the region is found. Regions belonging to the spokes and the region in the ring where the spoke intersects the ring are shown. All regions belonging to a spoke are identified with the same colour (see Fig. 9). All regions in the ring have been assigned a distance of 0 in both the plots.

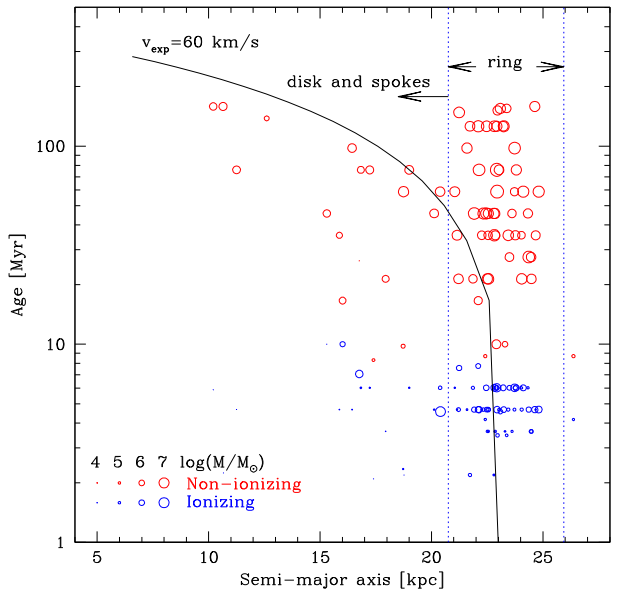

Figure 11. Ages of UV sources are plotted against their current distance from the centre of the ellipse that best matches the outer ring. This centre is the expected impact point. The ionizing young and non-ionizing old populations of each source are shown by empty circles of blue and red colours, respectively, with the sizes of the circles indicating the mass of the population following size code at the bottom-left corner of the plot. The oldest sources at each distance are consistent with a wave expansion velocity of 60 km s^{-1} (solid line).

traced in this figure, and named clockwise from north by letters SP-N (red), SP-NW (green), SP-W (blue), SP-SW (cyan), SP-S (pink), and SP-S (black). Recent simulation of Renaud et al. (2018) suggests that the spokes might be tracing the trajectory of the material falling back to the nucleus from the outer ring. Based on this suggestion, we measured the distance of a region to the outer ring along the traced spoke. In Fig. 10, we show the observed $F450W - K$, $F450W - F814W$, and FUV $- F450W$ colours plotted against this distance. Only the regions belonging to the spokes and the region in the ring where the spoke intersects the ring are shown. All regions belonging to a spoke are identified with the symbol of the same colour as the colour of the line used in Fig. 9 to delineate the spoke it belongs to. A colour gradient smoothly reddening away from the outer ring is best seen in the FUV $- F450W$ colour, with a similar trend in other colours also. The three regions farthest from the outer ring are the reddest. However, in the 10 kpc region internal to the ring, the gradient is shallow. It is worth to note that the range and dispersion in colours among the six points belonging to the ring (x-axis = 0 kpc) are similar to that of the regions in the 5 kpc zone immediately inside the ring, suggesting that the outer ring, which is easy to delineate in a Hα map (see Fig. 1, right), will not show up in a colour map. This behaviour illustrates again that the colours are dictated by the non-ionizing populations.

5.2 Scenario of star formation in the Cartwheel

The galactocentric distance of any point in the disc of a galaxy is measured as the semimajor axis of the ellipse fitted to the isophote that contains the point. The ellipse parameters, namely centre, ellipticity, and position angle are obtained by fitting the isophotes. In spiral galaxies, the ellipticity is a measure of inclination of the disc, which is constant for a non-warped disc, and the centre is the nucleus when present, or the centre of the bulge in general. Defining the ellipse centre for a collisional ring galaxy is non-trivial as it contains two centres: (1) the nucleus that defines the centre of the pre-collisional disc; and (2) the centre of the outer ring (the back cross in Fig. 9). Marston & Appleton (1995) fixed the nucleus as the centre for inner ellipses and varied the centre smoothly between the nucleus and the centre of the ring to define nine non-intersecting ellipses. The semimajor axis of the ellipse was taken as the galactocentric distance. We followed a similar approach to assign a galactocentric distance to our regions.

In Fig. 11, we plot the derived ages of the young ionizing and old non-ionizing populations in each UV-selected region against the galactocentric distance. The size of the symbols is scaled proportional to their masses in order to highlight the most prominent star forming events (see the legends at the bottom-left). The regions belonging to the ring are spread over galactocentric distances between 21 and 26 kpc, which is indicated by vertical blue lines. The age of the old population in the ring covers the entire range of the observed ages. On the other hand, spoke regions farther from the outer ring are systematically older. This trend is especially noticeable in the upper boundary of ages at each galactocentric distance. We show the distance travelled by an outwardly propagating star-forming wave of 60 km s^{-1} velocity by a solid line, which represents very well the upper boundary of the observed ages as a function of galactocentric distance. We discuss this trend in terms of the collisional scenario of ring formation below.

In the classical scenario of ring formation proposed by Lynds & Toomre (1976), the propagating density wave triggers star formation as it advances outwards, leaving behind successively older population of stars in its trail. The age of the oldest population at each radius would then indicate the epoch when the wave propagated at that radius. Once the star formation is triggered it can continue forming new generations of stars until the region runs out of gas or suffers

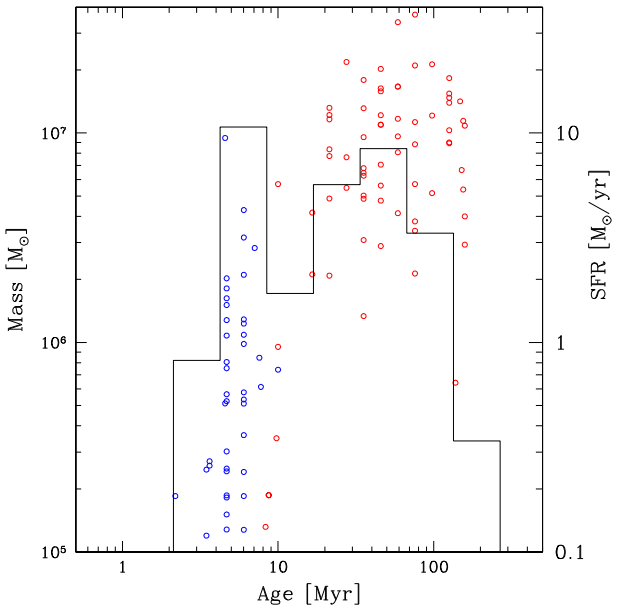

Figure 12. Star formation history of the Cartwheel galaxy using UV data. The mass (left *y*-axis) and SFR (right *y*-axis) of the young (blue circles) and old (red circles) populations are plotted versus the age.

from negative feedback effects of star formation (see e.g. Korchagin et al. 2001). Thus, at each galactocentric distance, a range of younger ages is expected. A comparison of the ages for the older populations in our study with the scenario of star formation triggered by a propagating density wave suggests that the upper boundary of ages at semimajor axis lengths between 10 and 20 kpc is in agreement with a propagating wave of 60 km s^{-1} velocity, a value consistent with the ring expansion velocity found by Higdon (1996) using H I gas. Thus, the UV-selected regions in the spokes trace star formation that got triggered by the passage of the expanding wave.

Fig. 11 shows that the outer ring contains populations formed over a wide range of ages, with the oldest populations as old as those along the spokes. The outer ring is not expected to contain populations older than a few tens of million years according to the classical density wave triggered star formation. This suggests that some of the populations that were formed in the inner parts of the disc during the passage of the density wave were dragged by the wave to their current location in the ring. Such a scenario has been suggested in the recent simulations of the Cartwheel-like galaxies by Renaud et al. (2018). The relative concentration of UV-selected old regions in the ring and along the spoke suggests that a major fraction of formed stars got dragged in the wave.

The availability of mass and age of the old and young star-forming events allows us to construct a detailed star forming history of the Cartwheel after it suffered the ring-making collision. In Fig. 12, we show the mass of the young and old populations as a function of their respective ages. We summed the masses of both the populations in bins of 0.5 dex ages to obtain an estimation for the star formation history in the Cartwheel. The results are shown by the solid histogram, with the SFR indicated in the right axis. At older ages, our detection limit prevents us detecting low-mass clusters, because of which the estimated past SFRs could be lower limits. We find an abrupt increase in star formation at 150 Myr, which continued at a steady SFR $\sim 5\ M_\odot\ yr^{-1}$ until ∼20 Myr ago. After a quiet period of 10 Myr, star formation became active again over the last 10 Myr, reaching a peak SFR $= 18\ M_\odot\ yr^{-1}$, which agrees excellently with the value derived by Mayya et al. (2005) using far-infrared, radio-continuum, and Hα luminosities. We remark that the size of the age bins is kept constant in logarithmic intervals, because of which our derived SFRs in the past are averages over periods much longer than 20 Myr. Hence, the dip and then a sudden increase in SFR seen over the last 20 Myr may be part of short-term fluctuations. Thus in summary, our analysis suggests that the Cartwheel was forming stars steadily over the last 150 Myr at SFR $\sim 5\ M_\odot\ yr^{-1}$.

6 CONCLUSIONS

We investigated the star formation history of the archetype collisional-ring galaxy Cartwheel. For this, we analysed new deep and high-resolution FUV images obtained with the *AstroSat*/UVIT mission in the FUV and publicly available optical and infrared images. Here we summarize our findings.

(i) The FUV emission of the Cartwheel is concentrated mainly in the star-forming outer ring. No trace of emission from the nucleus and inner ring is found.

(ii) We have identified 73 regions in the *AstroSat*/UVIT images of the Cartwheel, 58 of which are located in the outer ring. The remaining 15 regions belong to the spokes.

(iii) The UV sources in the ring contain more than one population of stars. The bulk of the FUV emission comes from non-ionizing stars with a range of ages ∼20–150 Myr.

(iv) The FUV regions located in the spokes have negligible current star formation. The age of the dominant older population increases with the distance from the outer ring.

(v) We find that the older populations in the ring have mass that is ∼25 times more than the population producing the ionization.

(vi) The ages for the older populations in our study suggest that the upper boundary of ages at galactocentric distances between 10 and 20 kpc is in agreement with a propagating wave of 60 km s^{-1} velocity, consistent with the ring expansion velocity obtained by Higdon (1996).

(vii) We report a SFR $= 5\ M_\odot\ yr^{-1}$ over the past 150 Myr, with an increase to $\sim 18\ M_\odot\ yr^{-1}$ in the recent 10 Myr consistent with Mayya et al. (2005).

We conclude that the UV-selected regions in the spokes trace the star formation that got triggered by the passage of the expanding wave. The range of ages of the stellar populations in the ring supports a scenario where some of the stars formed in the wave in the past were dragged along it to the current position of the ring following the scenario suggested by Renaud et al. (2018). Study of other ring galaxies (e.g. AM 0644−741) using the *AstroSat* and optical (e.g. VLT/MUSE and *HST*) data would be able explore whether the scenario presented here for the Cartwheel is applicable for other collisional ring galaxies.

ACKNOWLEDGEMENTS

We thank an anonymous referee whose comments have greatly helped in improving the presentation of this paper. We also thank CONACYT for the research grant CB-A1-S-25070 (YDM). This publication makes use of data from the Indian Space Research Organization's (ISRO) *AstroSat* mission, which is housed at the Indian Space Science Data Centre (ISSDC). The UVIT data used was processed at IIA by the Payload Operations Centre. The UVIT was developed in collaboration with IIA, IUCAA, TIFR, ISRO, and CSA. This research has made use of the NASA/IPAC Extragalactic Database (NED), which is operated by the Jet Propulsion Laboratory,

California Institute of Technology (Caltech) under contract with NASA.

DATA AVAILABILITY

Tables 2 and 3 contain all the astrometric and photometric data used in this work. The reduced fits files on which these data are based will be shared on reasonable request to the first author. The *AstroSat* UVIT data analysed is publicly available from the ISSDC Astrobrowse archive website: https://astrobrowse.issdc.gov.in/astro_archive/archive/Home.jsp

REFERENCES

Amram P., Mendes de Oliveira C., Boulesteix J., Balkowski C., 1998, A&A, 330, 881

Appleton P. N., Marston A. P., 1997, AJ, 113, 201

Appleton P. N., Struck-Marcell C., Bransford M. A., Charmandaris V., Marston A. P., Borne K., Lucas R., 1996, in Bender R., Davies R. L., eds, Proc. IAU Symp. 171, New Light on Galaxy Evolution. Kluwer, Dordrecht, p. 337

Barway S., Mayya Y. D., Robleto-Orús A., 2020, MNRAS, 497, 44

Calzetti D., Kinney A. L., Storchi-Bergmann T., 1994, ApJ, 429, 582

Calzetti D., Armus L., Bohlin R. C., Kinney A. L., Koornneef J., Storchi-Bergmann T., 2000, ApJ, 533, 682

Cardelli J. A., Clayton G. C., Mathis J. S., 1989, ApJ, 345, 245

Eldridge J. J., Stanway E. R., Xiao L., McClelland L. A. S., Taylor G., Ng M., Greis S. M. L., Bray J. C., 2017, Publ. Astron. Soc. Aust., 34, e058

Fosbury R. A. E., Hawarden T. G., 1977, MNRAS, 178, 473

Ghosh S. K., Tandon S. N., Joseph P., Devaraj A., Shelat D. S., Stalin C. S., 2021, J. Astrophys. Astron., 42, 29

Ghosh S. K. et al., 2022, J. Astrophys. Astron., 43, 77

González Delgado R. M., Cerviño M., Martins L. P., Leitherer C., Hauschildt P. H., 2005, MNRAS, 357, 945

Gordon K. D., Clayton G. C., Misselt K. A., Landolt A. U., Wolff M. J., 2003, ApJ, 594, 279

Hernquist L., Weil M. L., 1993, MNRAS, 261, 804

Higdon J. L., 1995, ApJ, 455, 524

Higdon J. L., 1996, ApJ, 467, 241

Korchagin V., Mayya Y. D., Vorobyov E., 2001, ApJ, 554, 281

Kroupa P., 2001, MNRAS, 322, 231

Kumar A. et al., 2012, in Takahashi T., Murray S. S., den Herder J.-W. A., eds, Proc. SPIE Vol. 8443, Space Telescopes and Instrumentation 2012: Ultraviolet to Gamma Ray. SPIE, Bellingham, p. 84431N

Lynds R., Toomre A., 1976, ApJ, 209, 382

McCall M. L., Rybski P. M., Shields G. A., 1985, ApJS, 57, 1

Marcum P. M., Appleton P. N., Higdon J. L., 1992, ApJ, 399, 57

Marston A. P., Appleton P. N., 1995, AJ, 109, 1002

Mayya Y. D., Prabhu T. P., 1996, AJ, 111, 1252

Mayya Y. D., Bizyaev D., Romano R., Garcia-Barreto J. A., Vorobyov E. I., 2005, ApJ, 620, L35

Mayya Y. D., Plat A., Gómez-González V. M. A., Zaragoza-Cardiel J., Charlot S., Bruzual G., 2023, MNRAS, 519, 5492

Osterbrock D. E., Ferland G. J., 2006, Astrophysics of Gaseous Nebulae and Active Galactic Nuclei, 2nd edn. University Science Books, Sausalito, CA

Renaud F. et al., 2018, MNRAS, 473, 585

Struck C., Appleton P. N., Borne K. D., Lucas R. A., 1996, AJ, 112, 1868

Tandon S. N. et al., 2017, AJ, 154, 128

Tandon S. N. et al., 2020, AJ, 159, 158

Willmer C. N. A., 2018, ApJS, 236, 47

Xiao L., Stanway E. R., Eldridge J. J., 2018, MNRAS, 477, 904

Zaragoza-Cardiel J., Gómez-González V. M. A., Mayya D., Ramos-Larios G., 2022, MNRAS, 514, 1689

This paper has been typeset from a TEX/LATEX file prepared by the author.